Aerodynamic Characteristics of CLARK-Y Smoothed Inverted Wing with Ground Effects

Ihsan Y. Hussain, PhD
Mech. Engr. Dept.
University of Baghdad
Iraq-Baghdad

Mustafa S. Abood
Mech. Engr. Dept.
University of Baghdad
Iraq-Baghdad

ABSTRACT
A two-dimensional computational study had been performed regarding aerodynamic forces and pressures affecting a cambered inverted airfoil, CLARK-Y smoothed with ground effects by solving the Reynolds-averaged Navier-Stokes equations, using the commercial software COMSOL Multiphysics 5.0 solver. Turbulence effects are modeled using the Menter shear-stress transport (SST) two-equation model. The negative lift (down-force), drag forces and pressures surface were predicted through the simulation of wings over inverted wings in different parameters namely; varying incidences i.e. angles of attack of the airfoils, varying the ride hide from the ground covering various force regions, two-dimensional cross-section of the inverted front wings to be fixed on nose of a race car- and varying speeds of initial airflow (Reynolds number). The results show that the down-force increases as the angle of attack increases; however, if an inverted wing is fixed on a car at high angles of attack the wing starts to stall which is not a desired condition that affects the vehicle stability and performance. As the ride height was reduced, the down-force was increased; at clearances between the suction surface and the ground of less than 0.2 of the chord length c, the down-force is significantly higher. Very close to the ground, at a ride height of less than 0.1c, down-force decreases as the wing stalls. Also, down-force increases as the free-stream velocity (Reynolds number) increases. The pressures for lower and upper surface of the wing increased with increasing both of angle of attack and ride height, but remains relatively ineffective with varying the speeds.

Keywords
Inverted Wing, Ground Effects, CFD, Aerodynamic Characteristics, CLARK-Y smoothed (clarkysm-il) Airfoil.

1. INTRODUCTION
There are three designing options for examining the aerodynamic characteristics of open-wheel racing series, such as Formula 1 and Indy Racing, or its bodywork parts: wind tunnel testing using a model, computational fluid dynamics (CFD) simulation, and track testing with a real vehicle. The latter is so rarely in the context of ongoing design development [1], and the previous two are usually carried out in close concern with CFD both filling in gaps in wind tunnel testing cannot be done in experimental conditions, in addition of the high cost of wind tunnel model and track-based testing [2].

While designing a race car the most important and significant sides the designer has to deal with, is the field of aerodynamics. The designer in the field of aerodynamic has two main concerns: the creation of down-force, negative lift, using inverted wings, to help the car steer onto the track and enhance cornering forces; and reducing the drag force, caused by turbulence which in turn reduces the speed of the car [3]. These elements improve the performance of the car.

The inverted front wing of the open-wheel racing car is the single so important aerodynamic component. This is because the front inverted wing of the car influences the airflow over the rest of the body because it is the part, which first comes in impact with the airflow. It also influences the flow of the air into the radiator, brake ducts and diffuser and also to the main engine intake.

Down-force is done by the front inverted wing due to the ground effect where more force is generated when airfoil is moving close to the ground surface. This is one of the many factors that are influenced by the front inverted wing. Although wind tunnel testing remains a significant tool for aerodynamic development, CFD plays an important role because of its efficient cost performance compared with tunnel testing, and the detailed flow information that is available [4].

The first computational investigations of an inverted wing in ground effect started in the 1980s. The earliest work was done by Katz [5] and Knowles et al. [6], using a potential flow-based panel method to simulate a single-element inverted wing in ground effect. Katz [5] noticed that as the airfoil got closer to the ground it generated more down-force. In the mid of 1990s, Ranzenbach and Barlow [7-8] performed a series of two-dimensional (2D) numerical investigations of wings in ground effect. A NACA 0015 airfoil at zero incidence was studied. The Reynolds number based on the chord was $1.5x10^6$. They used a multi-block structured grid of 20,000-30,000 points and the ground was modeled both as being stationary and moving. The results obtained compared well, showing a rise in down-force with a decrease in ride height until a maximum was reached and further reduction in ride height resulted in a drop in down-force. Moving ground tests gave a similar trend, but showed a much higher value of down-force at low ride heights, highlighting the significance of modeling a moving ground. In another study, Zerihan and Zhang [10] performed a Reynolds-averaged Navier–Stokes (RANS) simulation for a two-dimensional single-element airfoil, by using a fully structured grid with the Spalart–Allmaras [11] and shear stress transport (SST) k-ω turbulence models. Fully structured grids of up to 30,000 grid nodes were used. Both of them found that the down-force increases with reducing ground clearance until a maximum is reached, but in contrast to Ranzenbach and Barlow [7-9], they associated the force-reduction phenomena to the starting of stall. Mahon and Zhang [13] conducted a further computational analysis for the surface pressure and wake characteristics. A hybrid grid of around 350,000 cells was used. Various types of turbulence models were compared with the results of the experiments [10 & 12]. The results of the SST k-ω model showed the most accurate prediction of the pressure distributions and force slope. Van den Berg [15] extended the numerical work on Mahon's wing, using a fully structured grid of about 3.8 million points. He investigated seven turbulence models, selecting the Spalart-Allmaras model [11], and his simulations showed a good advance of the quantitative resulted data.

In a further analysis including PIV and LDA, Zhang et al.[16] showed that the edge vortex formed below the inverted wing has a secondary role in the down-force enhancement process and that changes in the rate of down-force variation is associated with the edge vortex breakdown. Kieffer et al. [17] examined effects of the incidence of a single element airfoil, modeling a Formula Mazda wing. The turbulence model was the standard *k*-ε model. The numerical results, however, were obtained by using a fixed ground boundary, and there was no experimental validation. Kamas [18] carried out computationally a two-dimensional and three-dimensional study regarding aerodynamic forces affecting a cambered wing, NACA2414 and a symmetric wing, NACA 0015. He predicted the negative lift (down-force) and the drag forces in the simulation of flow of air over inverted rear-wings in different configurations namely; two dimensional cross section of the inverted rear-wings to be fixed on back of a car -varying incidences i.e. angles of attack of the airfoils and varying speeds of initial airflow. He employed RANS equations, Spallart-Allmaras, and k-ε turbulence models using commercial airflow simulation software, CosmoFloWorks. The Reynold number of the flow based on the chord line was taken 2.01×10^6 in both cases. The free airflow velocities were set at 30, 35, 40, 45 and 50 m/s for the inverted rear-wings set at the higher incidences of 8, 12, and 16 degrees so as to illustrate the stall condition occurring at high level angles of attack. He concluded that the down-force increases as the angle of attack increases. Diasinos et al. [19] conducted a 3-D CFD study of the influence of wing span for an inverted wing with endplates with ground effect. The airfoil used was modified NASA GA(W) LS (1)-0413. They used a commercial finite-volume RANS equation solver, Fluent, to generate all results. Also, they constructed the numerical model to replicate the simulations with high fidelity and the freestream flow velocity was 30 m/s, giving a Reynolds number of approximately 4.6×10^5/m. The moving ground was represented at a velocity equal to the airflow. Three turbulence models were used for a comparison; the Spalart-Allmaras model, the realizable k-ε model, and the shear stress transport variant of the k-ω closure. They determined aerodynamic coefficients for different spans at different ground clearances. It was shown that, compared to a large-span airfoil, an airfoil with a shorter span might have a lower lift coefficient but can operate nearer to the ground before performance is affected adversely. Finally Keogh [20] investigated an isolated inverted wing in ground effect in four different flow conditions to identify the effects of cornering. They conducted a numerical analysis of the inverted T026 airfoil geometry through the curved path of a constant radius corner. Primary vortex behavior was noticed to differ significantly in both direction and structure. Fluent, a commercial finite-volume RANS solver, used as software solver, velocity of the fluid relative to the airfoil geometry was set at 30m/s, corresponding to a Reynolds number of $4.6\text{x}10^5$/m. As the tests were conducted with a moving ground, the ground was capable to be modelled as stationary relative to the free-stream fluid. He observed all of Effects of flow curvature, a velocity gradient and yaw to result in changes to the pressure surface distribution and the path of the prominent vortices generated at both ends of the span.

In the current investigation, a single element inverted airfoil in ground effect is computed using RANS simulation. The airfoil used is CLARK-Y smoothed type. The free stream velocity is variant 30, 35, 40, 45 and 50 m/s, corresponding to Reynolds numbers of 5.956×10^5, 6.949×10^5 7.941×10^5, 8.934×10^5 and 9.927×10^5, respectively, and the ride height (h/c) also was changing from 0.05 to 0.2 for different incidences from zero to 15°.The commercial software COMSOL Multiphysics 5.0 solver was used for solving RANS equation using finite element method. The Menter shear-stress transport (SST) two-equation turbulence model was used [21]. The focus of this investigation is on both pressures surface and the sectional forces flow field, since practice dictates that other aerodynamic components follow the front wing of a racing car.

2. AIRFOIL GEOMETRY

A sketch of the inverted single-element airfoil with the suction surface closer to the ground is shown in Figure 1. The airfoil is derivative of the CLARK-Y smoothed profile. The chord length *c*, distance between leading edge and trailing edge, is 300 mm. Maximum thickness is t/c=0.117. The incidence α, defined as the angle between the chord and the horizontal line, was positive for a nose down rotation. The ride height *h* is defined as the vertical distance between the lowest point on the suction surface of the airfoil and the ground plane, with the wing incidence set to zero degrees. The coordinate's origin is set at the nose of the airfoil. The axes were oriented such that *x* was aligned with the incoming flow and positive downstream to the right, and *y* was normal to the ground and positive up. For nomenclature purposes down-force, or negative lift, is considered positive when pointing down to the ground.

3. COMPUTATIONAL MODELING

3.1 Governing Equations and Turbulence Model

Computations are conducted by solving the two-dimensional steady RANS equations. A commercial RANS solver, COMSOL Multiphysics 5.0, which uses the finite difference method, is used here. In such configuration solutions at each iteration were obtained by solving the RANS equations for continuity and momentum:

$$\frac{\partial}{\partial x_j}u_j = 0 \quad \text{...} (3.1)$$

$$\frac{\partial u_i}{\partial t} + u_j\frac{\partial u_i}{\partial x_j} = -\frac{1}{\rho}\frac{\partial p}{\partial x_i} + \frac{\partial}{\partial x_j}\left(\vartheta\frac{\partial u_i}{\partial x_j} - \overline{\acute{u}_i\acute{u}_j}\right) \quad \text{................} (3.2)$$

Where x_i and x_j are the directional tensors in the *i*th and *j*th direction (i.e. $i = j = 1, 2= x, y$), u_i and u_j are the ensemble-averaged velocity tensors and *p* is the air pressure. ρ is the air density, was applied to simulations involving compressible flow although the effect of this modelling choice was not that great at such relatively low Mach numbers (M< 0.3) to assume incompressible flow, whereas ϑ kinematic viscosity is constant

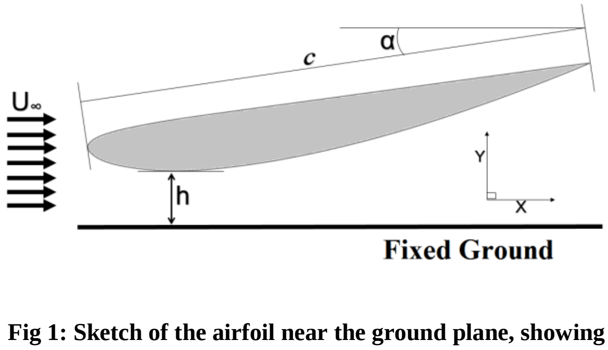

Fig 1: Sketch of the airfoil near the ground plane, showing the definition of airfoil chord c, ride height h, angle of attack α, and freestream velocity U_∞

values based on ISA. The Reynolds stresses ($-\overline{\acute{u}_i\acute{u}_j}$), which represent the effects of turbulence that they are modeled using the Menter shear-stress transport (SST) two-equation turbulence model [21]. Since Mahon and Zhang [13] compared various types of turbulence models using inverted wing profile. They showed that the SST *k*-ω model presents the best prediction at the ride height in pressure distributions and wake profiles.

3.2 Computational Grids

A multi-block hybrid grid design is used, containing both structured and unstructured blocks. Fine grid is needed in these regions to read flow properties. Triangular element with free mesh (default setting) is chosen to mesh the rectangular region (domain). The wall y+ value remained below 1 over the wing and ground (Figure 2b). The size of the computational domain has been examined between 5*c* and 20*c*. The chosen domain extends 1.7 chord lengths in front of and 5 chord lengths behind the wing's leading edge. The distance between the upper and lower boundaries is set as 2.33 *c*. The domain size were created to represent the 0.7×0.7×1.5 m wind tunnel of the Mech. Engr. Dept. / University of Baghdad. A schematic of the computational domain and grid is shown in Figure 2.

3.3 Boundary Conditions

The computational boundary conditions were configured to reproduce the experimental conditions. The upstream boundary was modeled using a freestream velocity inlet boundary condition. The corresponding inlet velocity was varied from 30 to 50 m/ s in a positive stream-wise direction.

The downstream boundary was modeled using a pressure exit boundary condition. The gauge pressure was set at zero. The top (tunnel ceiling) of the domain is defined with symmetry boundary conditions, which is equivalent to a zero-shear slip wall, so as to avoid the high grid density which would be required to resolve the wind tunnel boundary layer. This formulation was set in order to reproduce the experimental conditions imposed by the roof of the wind tunnel test section. The surfaces of the airfoil and ground were modeled as solid walls with a no-slip condition enforced. The ground surface was fixed to simulate the experimental study and get convergent results.

3.4 Simulation Procedures

COMSOL Multiphysics 5.0 includes a number of solvers for partial differential equation (PDE)-based problems. The present work used a stationary to solve PDE problem which was presented for linear and nonlinear problems. The stationary steps were split into sub steps, Newton method with only Jacobean related components are dependent procedure in this method of solution which can save both memory and time to solve.

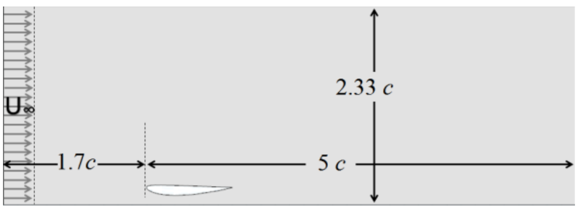

(a)

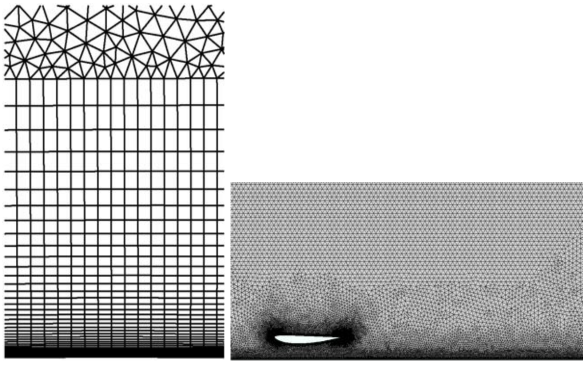

(b) **(c)**

Fig 2: Computational domain (a) schematic, (b) near wall grid, and (c) off-surface domains

Surface pressures, drag and lift coefficients are studied for various velocities, 30, 35, 40, 45, 50 m/s with varying the ride height, 0.05c, 0.1c, 0.15c and 0.2c m, and the angle of attack, 0, 5, 10, 15 degrees. The convergence criteria for all simulations are carefully monitored, allowing the numerical residuals to decrease by O (10^{-4}). For the two-dimensional study, the number of cells is examined between 13,000 cells and 120,000 cells, and the grid of 50,000 cells is chosen; the difference between the finer and selected grids is less than 0.1%. Where the coarse, fine and finer meshes examined for random case to predict data for comparing. Cells were primarily concentrated at the boundary.

As can be seen in Table 1 the three types of meshes under-predicted lift and over-predicted drag in comparison, with minor differences between. Figure 3 shows no real difference in terms of the pressure distribution prediction with chord-wise of the examined meshes. For the steady RANS simulations, the flow was initialized using the inlet conditions, and the solution was iterated until convergence was attained. This was reached when the force coefficients did not change with further iterations and required approximately 100 iterations.

Table 1. Validation against lift and drag values for different mesh sizes

Mesh type	C_L	C_D
Coarse	1.1885	0.064511
Fine	1.4154	0.052353
finer	1.4576	0.051197

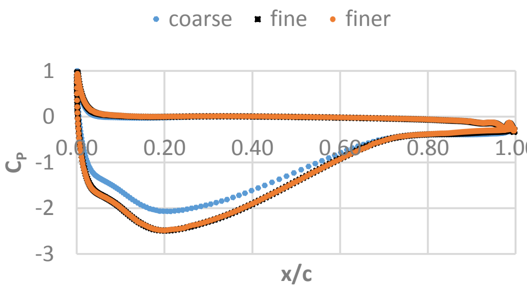

Fig 3: Wing surface pressure distributions for coarse, fine and finer meshes

4. RESULTS AND DISCUSSION

In this section, the trends of wing down-force with ride height, angle of attack and velocity are analyzed, followed by an investigation into the flow physics responsible for this trends by using results of surface chord-wise pressures distribution.

Generally, all the results are presented in three levels (maximum, medium and minimum levels). Each parameter will be presented at three different values of the other variables, which represent the highest, middle and lowest values. For example: when studying the effect of ride height on the negative lift coefficient, the results are represented in three levels. Maximum level is at v = 50 m/s, $\alpha = 15^o$ and h/c = 0.2. Medium level is at v = 40 m/s, $\alpha = 10^o$ and h/c = 0.1 and minimum level is at v = 30 m/s, $\alpha = 0^o$ and h/c = 0.05.

4.1 Sectional Forces Analysis

4.1.1 Ground Effect at Reference Incidence

The down-force (negative lift) and drag coefficients vs the ride height is varied for different speeds at 0^o, 10^o and 15^o angles of attack are given in Figures 4 (a, b, c, d, e and f). With the airfoil in proximity to the ground, the effect of higher down-force coefficients can be seen clearly. The physical effects of the ground is to constrain the airflow over the suction surface of the airfoil. This causes an acceleration of the flow, if compared with the case out of ground effect and results in a greater suction on the suction surface, and hence a higher down-force. As the ride height is reduced, the ground effect causes the flow to be accelerated to a higher degree, generating a significantly higher down-force, as can be seen in figure 4 (a). At ride heights of less than approximately 0.2c, there is a gradual, and then significant deviation from the previous trend of ever increasing down-force with reduction in ride height. Indeed, the down-force falls off, to reach a maximum C_L of 0.884, at a ride height of 0.08c. Closer to the ground than this point, the down-force reduces significantly compared with the maximum (the force reduction phenomenon).The additional results can also be seen in Figure 4(a). The curves at the three velocities are very similar, the main difference occurring near to the force reduction phenomenon, where the test at the higher speed shows higher down-force values, but a similarly shaped curve. The maximum down-force occurs at the same height of 0.08c, but at a C_L of 0.939 for v=40 m/s and 0.968 for v= 50 m/s compared with 0.884 for the 30 m/s case.

Figure 4(d) also shows the effect of ride height on the drag of the wing. It has been shown that as the ride height is reduced, the down-force increases until the beginning of the force reduction phenomenon. This contributes to the induced drag of the wing. As boundary layer separation occurs at heights above the force reduction height, downwards this also contributes to the drag. These two factors are the reasons for the drag of the wing increasing with reducing the ride height. The drag consistently being higher for the lower velocity case.

Figure 4(b) presents the effect of ride height on the down-force, when the tests were performed at incidence of 10^o. The coefficient of the down-force slightly increases with increasing the ride height till the maximum value of 1.6226 for the velocity of 50 m/s. The maximum down-force occurs at the same height of 0.2c, with C_L of 1.5672 for v=30 m/s and 1.6037 for v= 40 m/s.

The effect of ride height on the drag of the wing at a reference incidence of 10^o is shown in figure 4(e). As the proximity to the ground is increased, the drag force increases to be the maximum value of 0.12414 for the velocity 30 m/s at ride height of 0.05, which is the same for the other three velocities (C_D= 0.12245 for 40 m/s and C_D= 0.12152 for 50 m/s).

For the figures 4(c) and 4(f), they are not much differing from the Fig 4 (b and e) in description. But can be seen the effect of separation is very clear at the angle of attack of 15^o where the maximum C_L= 1.5616 for v=40 m/s. at h/c=0.2.

4.1.2 Ground Effect Variation with Incidence

The variation of down-force with ride height for incidences of 0, 10 and 15^o at reference speed is presented in Figure 5. For the lowest ride heights at the h/c=0.05 the force reduction phenomena can be seen at zero angle of attack for the three velocities cases. Figures 5 (a) to (c) show the negative lift vs ride height curves for differing angles of attack. Of note is the trend of the post-stall (boundary layer separation) curves at 10^o and 15^o, similar in shape, showing increasing down-force coefficient with increasing ride height, contrary to the expected pre-stall trend of decreasing down-force coefficient with increasing ride height.

The drag coefficient for all velocity cases follows the same general trend. The trend of increased drag with decreased ride height for different angles of attack is visible in Figure 5. (d to f). Variation in ride height had an effect on the magnitude of the coefficient, but not the general trend.

4.1.3 Velocity Variation at Reference Ground Effect

Velocity in a typical road or street course, race-car speeds may vary from as low as 60 km/h to upwards of 280 km/h. With this extreme change in conditions, performance of an airfoil can vary greatly. Therefore, it becomes important to quantify the effects that speed, or Reynolds number, has on performance of a race-car airfoil. Figure 6 shows the effect of velocity on down-force curves and drag coefficient for the CLARK-Y smoothed (clarkysm-il) configuration at three reference ride height cases. As velocity or Reynolds number increases, lift coefficient increases and drag coefficient slightly decreases for the tested values of velocities. Typical increases in negative lift coefficient for an increase in velocity from 40 m/s to 50 m/s averaged 2.5%, while an increase in velocity from 30 m/s to 40 m/s caused an average increase in C_L of 1.9%. Figure 6(c) shows the curves of down-force with angle of attack for different velocities at h/c =0.2. It can be seen there is a reduction in C_L for the v=50 m/s curve between the approximate angle value of 6^o to 9^o then return to increase to be in a value less than the maximum value for velocity of 40 m/s curve. For the figures 6. (a and b) they are similar in behavior where the values of C_L not much varies with velocity change for the used values. For the C_D trends, see figure 6 (d, e, f) they are not much differ from the C_L trends but inversely proportional to the velocity and angle of attack.

4.2 Surface Pressures Distribution

4.2.1 Ground Effect at Reference Incidence

To investigate the effects of ride height variation. Calculations were performed at h/c=0.05, 0.1 and 0.2 and data concerning the surface pressures and sectional forces was extracted. Accordingly the realizable k−ω SST model was used in the simulations at various ride heights. The calculated surface pressures are presented data in Figure. 7. Figures7(a), (b) and (c) present the surface pressures for high, medium and low ride heights for three cases using $\alpha=0^o$ and v=30 m/s,$\alpha=10^o$ and v=40 m/s , $\alpha=15^o$ and v=50 m/s ,respectively, using the realizable k−ω SST turbulence model. As the ride height is reduced, the peak velocity on the suction surface increases. In close proximity to the ground, less than h/c = 0.1, regions of flow separation can be seen at the trailing edge, represented by the constant pressure region, initially small, but increasing in size with reducing the ride height. The stream-wise location of stagnation on the wing was found to move upstream with reducing ride height, decreasing from x/c=0.01 at h/c=0.2 to x/c=0.01 at h/c=0.05.The surface pressures on the pressure surfaces of the inverted wing remain relatively independent of ride height, when compared to the suction surface pressures, and were accurately predicted for all ride heights. A comparison of pressure distribution at $\alpha=10^o$ and v=40 m/s is made of the wing for different ride heights, see Figure. 7 (b). The pressures on the pressure surface of the inverted wing also remain relatively independent of ride height, whereas the pressures generated on the suction surface slightly increases with the ride height. On the suction surface, the suction peak for the wing at x/c=0.08 remains at the same place for h/c=0.1 and h/c=02. But the suction peak for the wing at h/c=0.05 situated at x/c=0.18.This will be known as the suction peak. Figure 7(c) shows that the pressure distribution at $\alpha=15^o$ and v=50 m/s for different ride heights. The surface pressures are identical for three ride heights and the suction surface only differs in the suction peak value which increases with increasing the h/c. The flow separation started at location of x/c=0.46 for h/c=0.2 and the separation becomes earlier with decreasing the ride height.

4.2.2 Ground Effect Variation with Incidence

The effect of angle of attack variation is investigated. Calculations were performed at α=0, 10 and 15^o to extract data about surface pressures and suctions. The calculated surfaces pressures data are presented in figure 8. Figures 8(a, b and c) present the surface pressure for three cases, in first case h/c=0.05 and v=30 m/s and in second case h/c=0.1 and v=40 m/s in third case h/c=02 and v=50 m/s, using the same previous procedure. As the angle of attack is reduced, the peak velocity on the surface decreases. In higher angles of attack, more than 10^o, regions of flow separation can be seen at trailing edge for all three cases, as for figure 8(a) initially small for α=0 occurs at x/c=0.833, but being more clear and earlier to happen with increasing the angle of attack, for α=10 separation occurs at x/c=0.5 and for $\alpha=15^o$ separation occurs at x/c=0.38. The stream-wise of stagnation on the inverted wing was found to move upstream with increasing angle of attack for all three cases, but at x/c=0.001 for $\alpha=0^o$, x/c=0.04 for $\alpha=15^o$. The surface pressure on the pressure side of the wing increases with increasing angle of attack also for all three cases. Figure 8(b) shows a comparison of pressure distribution at h/c=0.1 and v=40 m/s for different angles of attack. The suction peak moves instream wise with increasing the angle of attack from 0^o at x/c=0.002 to 15^o at x/c=0.03. As for figure 8(c) shows pressure distribution with chord-wise at h/c=0.2 and v=50 m/s for different angles of attack. The main difference between the first case and the other two cases is the flow separation of fluid occurs near the trailing edge at x/c of 0.98 and the suction peak is very small compared with the other angles of attack and located at x/c of 0.008.

4.2.3 Velocity Variation at Reference Ground Effect

The variation of velocity and its effect on the surface pressure is shown in figure 9. The calculations were performed at v=30, 40 and 50 m/s at reference values of ride height and angle of attack. The three figures 9(a, b and c) indicate the three cases of varying the references for different velocities in each case. From the figures it can be seen that the surface pressures, suction peak and separation of fluid flow remain relatively independent of velocity, when the three curves are approximately identical. Whereas the suction surfaces of the wing slightly creases with increasing the velocity for all three cases.

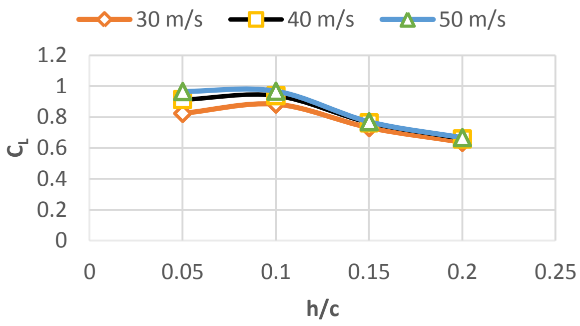

(a): at 0^o reference angle of attack

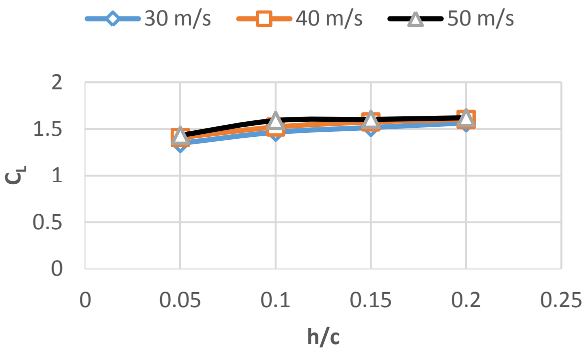

(b): at 10^o reference angle of attack

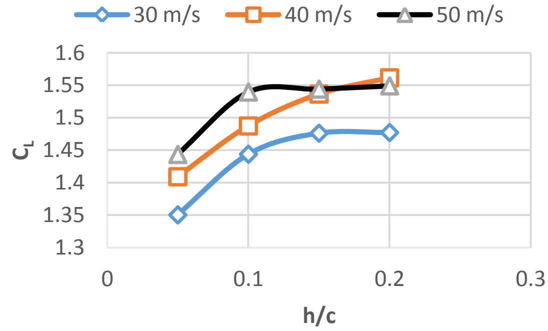

(c): at 15^o reference angle of attack

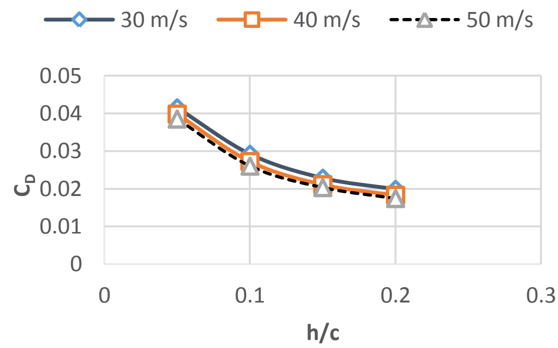

(d): at 0^o reference angle of attack

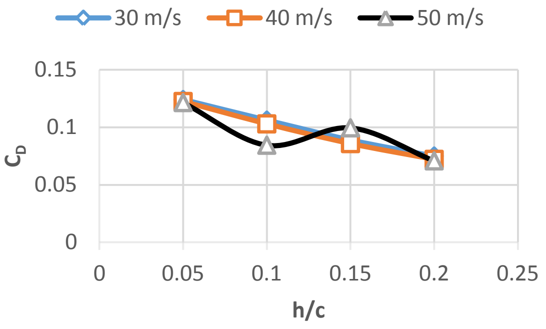

(e): at 10° reference angle of attack

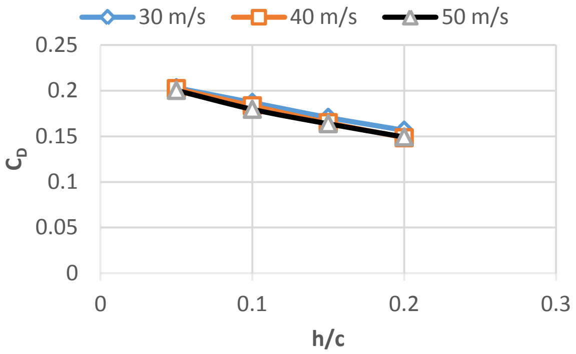

(f): at 15° reference angle of attack

Fig 4: Coefficient of negative lift and drag variation with ride height at reference angle of attack for set of speeds

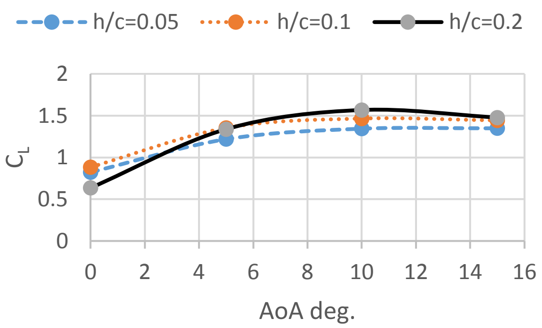

(a): at 30 m/s reference velocity

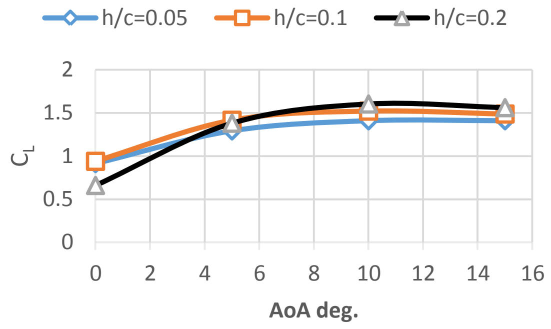

(b): at 40 m/s reference velocity

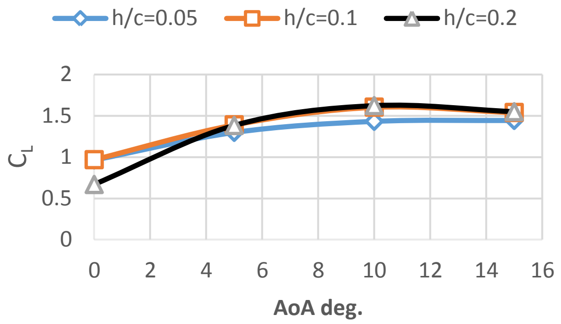

(c): at 50 m/s reference velocity

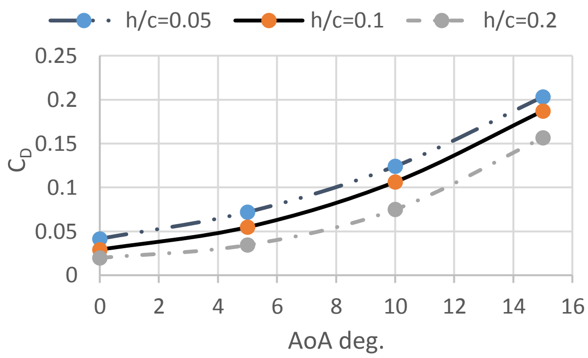

(d): at 30 m/s reference velocity

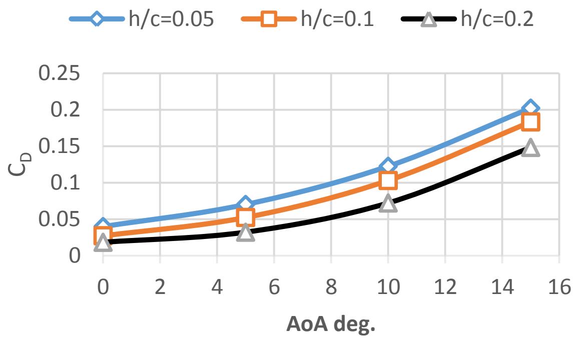

(e): at 40 m/s reference velocity

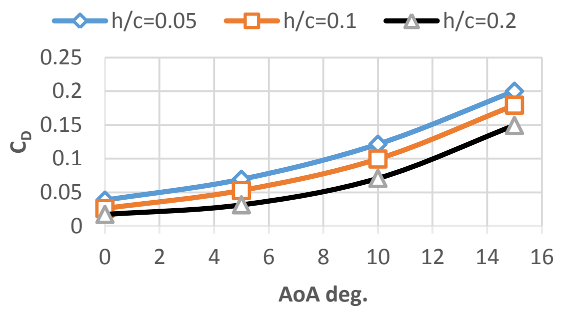

(f): at 50 m/s reference velocity

Fig 5: Coefficient of negative lift and drag variation with angle of attack at reference speed for set of ride heights

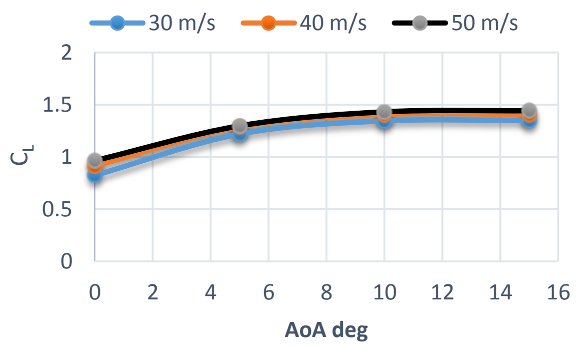

(a): at 0.05c reference ride height

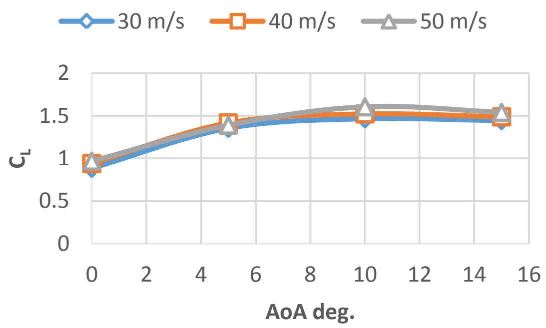

(b): at 0.1c reference ride height

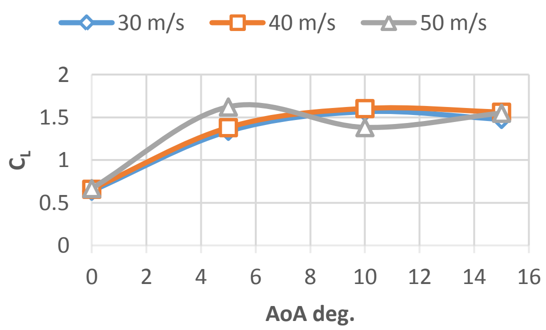

(c): at 0.2c reference ride height

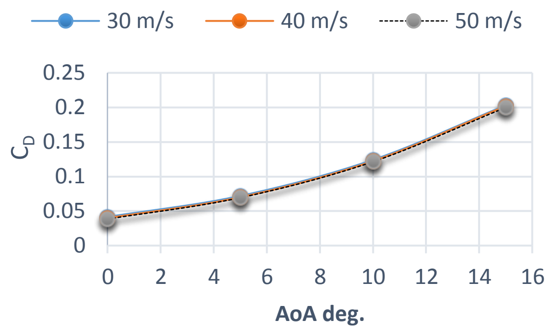

(d): at 0.05c reference ride height

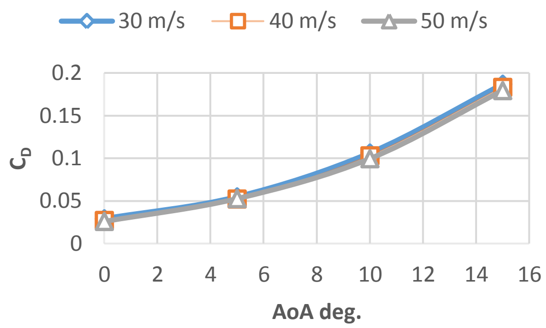

(e): at 0.1c reference ride height

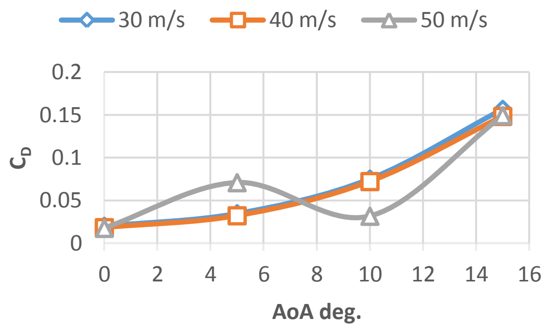

(f): at 0.2c reference ride height

Fig 6: Coefficient of negative lift and drag variation with angle of attack at reference ride height for set of speeds

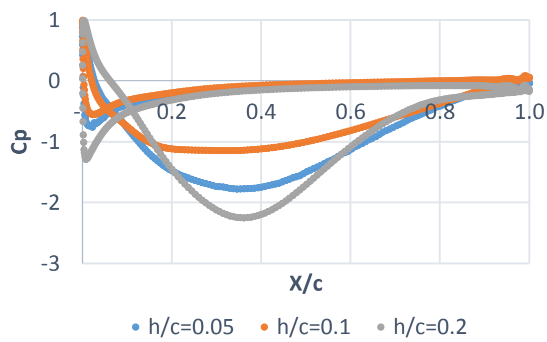

(a): at 0^o reference angle of attack and at 30 m/s reference velocity

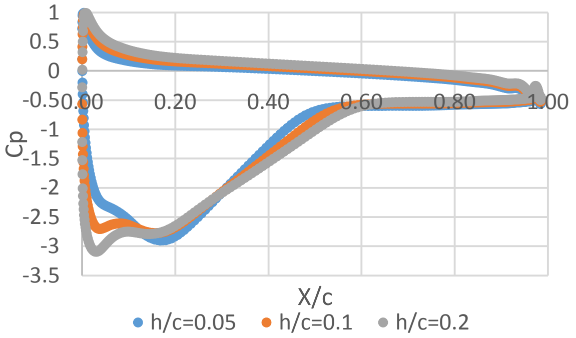

(b): at 10° reference angle of attack and at 40 m/s reference velocity

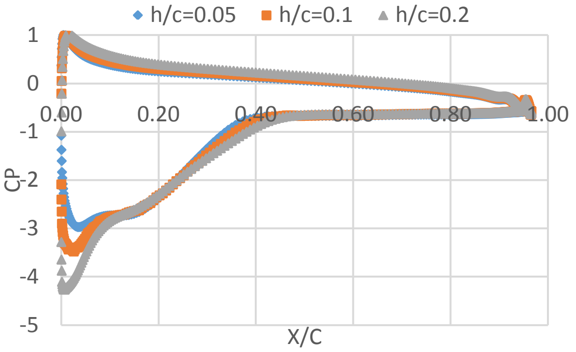

(c): at 15° reference angle of attack and at 50 m/s reference velocity

Fig 7: Pressure coefficient variation of lower and upper surfaces at reference speed and angle of attack for different ride heights

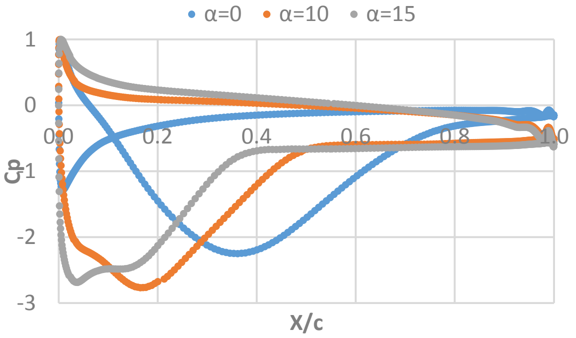

(a): at 0.05c reference ride height and at 30 m/s reference velocity

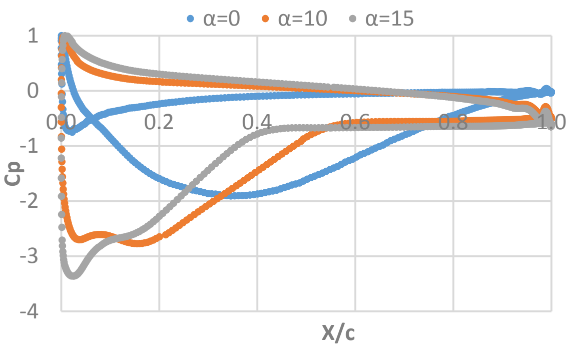

(b): at 0.1c reference ride height and at 40 m/s reference velocity

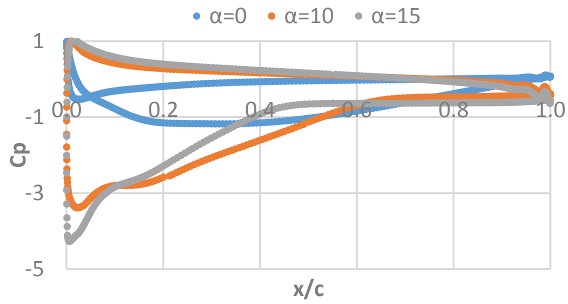

(c): at 02c reference ride height and at 50 m/s reference velocity

Fig 8: Pressure coefficient variation of lower and upper surfaces at reference speed and ride heights for different angles of attack

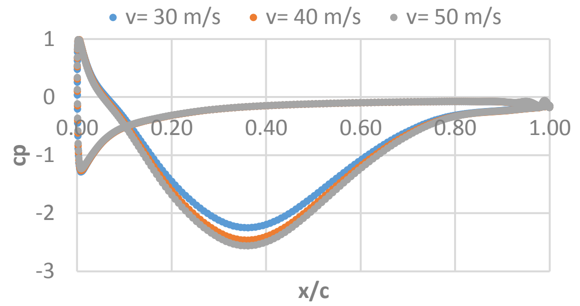

(a): at 0.05c reference ride height and at 0° reference angle of attack

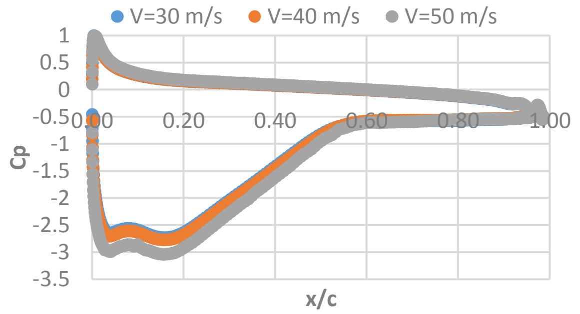

(b): at 0.1c reference ride height and at 10orefernce angle of attack

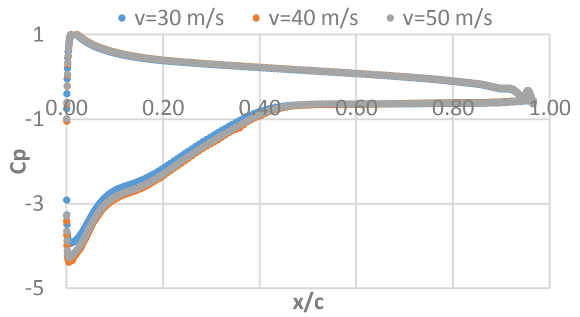

(c): at 0.2c reference ride height and at 15o reference angle of attack

Fig 9: Pressure coefficient variation of lower and upper surfaces at reference angles of attack and ride heights for different speeds

5. CONCLUSIONS

Single element inverted airfoil CLARK-Y smoothed is simulated at different ground proximity, at different angles of attack and at different speeds (Reynolds numbers) through the commercial flow work software Multiphysics COMSOL.

The present numerical investigation shows significant effects of angle of attack, free stream velocity and ride height on aerodynamic characteristics, these conclusions can be summarized as follows:

- The negative lift coefficient is increases as the ground clearance decreases from the wing. Force reduction phenomena occurs due to combination of both the minimum loss of negative lift to flow separation and the maximum gain in suction surface due to small ground clearance less than 0.1c.
- The drag coefficient increases as the ground clearances decreases.
- Improvement is found for the lift and drag forces when the airfoil at 5^o angle of attack and at 0.2c ground clearance for all tested velocities.
- Separation of the boundary layer occurred close to the trailing edge of the suction surface, at a higher angles of attack, larger than 10^o, and at a moderate ride height.
- Increasing the wing incidence, caused an increasing in negative lift, drag and the pressures surface for the upper and lower surface of the wing
- The velocity effects were least significance, with changes in negative lift, drag and the pressures for the upper and lower surface of the wing for the speeds range tested.
- The pressures along upper and lower surface of the airfoil increases in the ground proximity and angle of attack, but relatively remain ineffective with velocity change for the tested speeds range.

6. ACKNOWLEDGMENTS

The authors would like to thank Dr.Anmar Hamid Ali, a lecturer at the Mech. Engr. Dept., for his support: in using Multiphysics COMSOL 5.0 software.

7. REFERENCES

[1] Zhang, X., Toet, W., and Zerihan, J., 2006, “Ground Effect Aerodynamics of Race Cars,” Appl. Mech. Rev., 59, pp. 33–49.

[2] Toet, W. (2013) 'Aerodynamics and aerodynamic research in Formula I', The Aeronautical Journal, Vol. 117, No. 1187, pp.l-26.

[3] Mohd Syazrul Shafiq B Saad (2010), “Study of F1 Car Aerodynamics Front Wing Using Computational Fluid Dynamics (Cfd)”, University Malaysia Pahang, December.

[4] Aniruddha Patil, Siddharth Kshirsagar and Tejas Parge." Study of Front Wing of Formula One Car Using Computational Fluid Dynamics", ISSN 2278 – 0149 www.ijmerr.com Vol. 3, No. 4, October 2014.

[5] Katz, J., 1985, “Calculation of the Aerodynamic Forces on Automotive Lifting Surfaces,” ASME J. Fluids Eng. 107, pp. 438–443.

[6] Knowles, K., Donoghue, D. T., and Finnis, M. V., 1994, “A Study of Wings in Ground Effect,” Proceedings of the Loughborough University Conference on Vehicle Aerodynamics, Vol. 22, pp. 1–13.

[7] Ranzenbach, R., and Barlow, J.B., "Two-dimensional airfoil in ground effect, an experimental and computational study," 1994, Society of automotive engineers, Paper 94-2509.

[8] Ranzenbach, R., and Barlow, J.B., "Cambered airfoil in ground effect - an experimental and computational study," 1996, Society of automotive engineers, Paper 96-0909.

[9] Ranzenbach, R., and Barlow, J.B., "Multielement airfoil study," 1997, Society of automotive engineers, Paper 97-2238.

[10] Zerihan, J.D.C. and Zhang, X., "Aerodynamics of a single element wing in ground effect," Journal of Aircraft, Vol. 6, 2000, pp. 1058-1064.

[11] Spalart, P. R., and Allmaras, S. R., 1992, “A One-Equation Turbulence Model for Aerodynamic Flows,” AIAA Paper No. 1992-0439.

[12] Zhang, X., and Zerihan, J., 2003, “Off-Surface Aerodynamic Measurements of a Wing in Ground Effect,” J. Aircr., 40(4), pp. 716–725.

[13] Mahon, S., and Zhang, X., 2005, “Computational Analysis of Pressure and Wake Characteristics of an Aerofoil in Ground Effect,” ASME J. Fluids Eng., 127, pp. 290–298.

[14] Mahon, S.A., The aerodynamics of multi-element wings in ground effect, Ph.D. thesis, University of Southampton, Southampton, UK, 2005.

[15] Van den Berg, M.A., Aerodynamic interaction of an inverted wing with a rotating wheel, Ph.D. thesis, University of Southampton, Southampton, U.K., 2007.

[16] Zhang, X., Zerihan, J.D.C., Ruhrmann, A. and Deviese, M., "Tip vortices generated by a wing in ground effect," Tech. rep., 11th International Symposium: Applications of Laser Techniques to Fluid Mechanics, 2002.

[17] Kieffer, W., Moujaes, S., and Armbya, N., 2006, “CFD Study of Section Characteristics of Formula Mazda Race Car Wings,” Math. Comput. Model. Dyn. Syst., 43, pp. 1275–1287.

[18] Tuncay Kamas. "2-D and 3-D Assessment of Cambered and Symmetric Airfoils: A CFD Study", A thesis presented to the Graduate School of Clemson University, December 2009.

[19] Sammy Diasinos, Tracie J Barber and Graham Doig. "Influence of wing span on the aerodynamics of wings in ground effect". Journal of Aerospace Engineering, 227(3).569-573, March 2013.

[20] James Keogh, Graham Doig, Tracie J. Barber, Sammy Diasinos." The Aerodynamics of a Cornering Inverted Wing in Ground Effect", Science Faculty, Department of Engineering, Macquarie University North Ryde NSW 2109, Australia, 2013.

[21] Menter, F. R., 1994, “Two-Equation Eddy-Viscosity Turbulence Models for Engineering Applications,” AIAA J. 32(8), pp. 1598–1605.